NJC

Accepted Manuscript

This is an *Accepted Manuscript*, which has been through the Royal Society of Chemistry peer review process and has been accepted for publication.

Accepted Manuscripts are published online shortly after acceptance, before technical editing, formatting and proof reading. Using this free service, authors can make their results available to the community, in citable form, before we publish the edited article. We will replace this *Accepted Manuscript* with the edited and formatted *Advance Article* as soon as it is available.

You can find more information about *Accepted Manuscripts* in the Information for Authors.

Please note that technical editing may introduce minor changes to the text and/or graphics, which may alter content. The journal's standard Terms & Conditions and the Ethical guidelines still apply. In no event shall the Royal Society of Chemistry be held responsible for any errors or omissions in this *Accepted Manuscript* or any consequences arising from the use of any information it contains.

ROYAL SOCIETY OF CHEMISTRY

www.rsc.org/njc

Journal Name

ARTICLE

Improved performance of rare earth doped $LiMn_2O_4$ cathodes for lithium-ion battery applications

Received 00th January 20xx,
Accepted 00th January 20xx

DOI: 10.1039/x0xx00000x

www.rsc.org/

Pura Ram[a,#], Attila Gören[b,c,#], Stanislav Ferdov[b], Maria M. Silva[c], Rahul Singhal[d], Carlos M. Costa[b,c,*], Rakesh Kumar Sharma[a,*] and Senentxu Lanceros-Méndez[b,e,f]

Different rare-earth elements (Dy, Gd, Tb and Yb) doped $LiMn_2O_4$ spinel active material were prepared by sol-gel method. The rare earth doping elements decrease particle size but do not affect the formation of cubic spinel structure. Further, these dopants have strong influence in the overall electrical properties of the cathodes prepared from them. In the cyclic voltammetry measurements, two pairs of separated redox peaks are observed, independently to dopants. $LiMn_2O_4$ doped gadolinium (Gd) and dysprosium (Dy) exhibit a comparable room temperature rate capability to pristine $LiMn_2O_4$ with discharge capacity of 94.5 mAh g^{-1} and 82.3 mAh g^{-1}, respectively, versus 73.4 mAh g^{-1} for pristine $LiMn_2O_4$ at a rate of C5. Terbium (Tb) and ytterbium (Yb) doping show, on the other hand, lower performance. After 50 cycles at C2, the capacity fade is 7% for $LiMn_{1.95}Dy_{0.05}O_4$ and 14% for $LiMn_{1.95}Gd_{0.05}O_4$, whereas for $LiMn_2O_4$ it is 32%. The improved cycling performance of $LiMn_2O_4$ doped with Gd and Dy is attributed to the powder size and atomic radius of the elements. Differences of the capacity retention on cycling are attributed to superior structural stability due to rare earth doping. These results indicate that improved cathode materials doped with rare earth element are suitable for lithium-ion battery applications.

Introduction

There exist a global demand to develop clean, sustainable, renewable and environment friendly energy technologies as an alternative to traditional hydrocarbon fuels [1, 2]. The most important renewable energy types are solar, wind, geothermal and bioenergy [3]. The different types of renewable energy are very attractive but the efficient storage of the generated energy is one of the most critical issues to be resolved.

The accelerated technological advances in portable electronic products (mobile phones, computers, e-labels, e-packaging and disposable medical testers, among others) as well as in hybrid electric vehicles (PHEVs) and electric vehicles (EVs), lead to an increasing demand for higher battery autonomy as one of the main energy storage system [4].

Lithium-ion batteries present many advantages in comparison to other battery types, such as Ni-Cd [5-7], as they are lighter and cheaper, show high specific density: 100-265 Wh kg^{-1}, suitable power/weight relation (1800 W/kg) and large number of charge/discharge cycles.

The most important issues for improving lithium-ion battery performance are specific energy, power, safety and reliability. With respect to the three main components (anode: negative electrode [8], cathode: positive electrode and separator) of lithium-ion batteries, the cathode material is particularly relevant because it determines the cell capacity [9, 10].

Cathode electrode films are typically composed by a polymer binder, conductive additive and active material that is responsible for the cell capacity and cycle life through its high electrochemical reactivity [11, 12].

Lithium transition metal oxides ($LiMO_2$, M=Co, Ni, Mn; $Li_4Mn_5O_{12}$ [13]; lithium cobalt oxide ($LiCoO_2$)) [14], lithium manganese oxide ($LiMn_2O_4$) [15, 16] and Lithium transition metal phosphates ($LiMPO_4$, M=Mn, Co, Ni and Fe) [17] are mainly used active materials for cathode films.

[a] Department of Chemistry, Indian Institute of Technology Jodhpur, 342011, Rajasthan, India. Email: rks@iitj.ac.in
[b] Departamento/Centro de Física, Universidade do Minho, Campus de Gualtar, 4710-057 Braga, Portugal. E-mail: cmscosta@fisica.uminho.pt
[c] Departamento/Centro de Química, Universidade do Minho, Campus de Gualtar, 4710-057 Braga, Portugal.
[d] Department of Physics and Engineering Physics, Central Connecticut State University, New Britain, CT, 06067, USA.
[e] BCMaterials, Parque Científico y Tecnológico de Bizkaia, 48160-Derio, Spain
[f] IKERBASQUE, Basque Foundation for Science, Bilbao, Spain
# equal contribution.

For the first generation of plug-in hybrid electric vehicles or electric vehicles, $LiMn_2O_4$ cathodes have been applied taking into account its advantages: low toxicity, low cost, high thermal stability, high voltage >4V and environmental friendliness in comparison with other lithium transition metal oxides [18-20].

$LiMn_2O_4$ shows 3-dimensional channels in a cubic spinel structure (space group Fd3m) in which oxygen ions occupy the 32e position, Mn ions are located in the 16d site and Li in the 8a site [21].

Cathodes based on $LiMn_2O_4$ show high capacity fading in the charge/discharge process due to large Jahn-Teller (JT) instability caused by Mn^{3+} (loss of Mn through disproportionation of trivalent Mn) at the octahedral sites and Mn dissolution into the electrolyte solution [19, 22, 23].

The control of the morphology of the $LiMn_2O_4$ particles is very relevant for improving materials performance and spinel $LiMn_2O_4$ hollow nanocones seem to be a promising cathode material [24].

To reduce the capacity fading of $LiMn_2O_4$ and improve its electrochemical properties it is necessary to dope the structure with different elements (metals (such as: Al [25], non-metals, rare earth metals) [19], decrease the particle size [26] or perform surface coating [27].

The use of rare-earth or lanthanide elements that substitutes the Mn^{3+} ion reduces the capacity fading but also decreases the theoretical specific capacity of doped $LiMn_2O_4$. In this context, the use of rare earth metals as dopants for $LiMn_2O_4$ seems to be promising but it has been poorly addressed, the state of the art just reporting on the effect of gadolinium [28], dysprosium [29], lanthanum [30], cerium [30], neodymium [30], samarium [30] and terbium doping [31].

It has been observed that gadolinium doping decreases the cell dimension accompanied by the expansion of the LiO_4 tetrahedra and contraction of the MnO_6 octahedra, resulting in an improvement in the high-rate performance and lower capacity fading, respectively [28].

It was been demonstrated that Dy doping of $LiMn_2O_4$up to 0.05 ($LiMn_{2-x}RE_xO_4$; x=0.05) results in suitable capacity with good capacity retention [29]. Further, $LiMn_2O_4$doping with 0.05 of lanthanum, cerium, neodymium and samarium also improves the electrochemical properties of $LiMn_2O_4$ [30].

Terbium doping of $LiMn_2O_4$ particles leads to excellent rate capability with larger capacity and lower overpotential, relatively to undoped $LiMn_2O_4$, which results in improved power density [31].

Taking into account the effect of rare earth metals in the $LiMn_2O_4$ crystal structure (cell dimension and atomic arrangements) and its electrochemical performance, the main goal of this work is to produce $LiMn_2O_4$ particles doped with different rare earth elements -gadolinium (Gd), terbium (Tb), dysprosium (Dy) and ytterbium (Yb)- and evaluate the effect for the same rare-earth quantity (0.05). The effects of of rare-earth doping element (i.e, atomic number and size) on crystal structure and electrochemical performance (impedance spectroscopy, cyclic voltammetry and charge-discharge results) were analyzed.

Experimental

Synthesis of active material

The new spinel cathode materials of $LiMn_{2-x}RE_xO_4$ (x=0.05) and $LiMn_2O_4$ were synthesized via sol gel route with analytical grade chemicals. Stoichiometric mixtures of lithium acetate, manganese acetate, gadolinium acetate, terbium acetate, dysprosium acetate and ytterbium acetate were obtained in stoichiometry ratio all from Alfa Aesar, USA. The raw powders were subjected to heating treatment to reach phase purity and stable form of the materials.

Each constituent was dissolved in 2-ethylhexanoic acid to get a homogeneous solution at temperature 100-150 ºC for 30 minute and magnetic stirring rate of 200-300 rpm. After ensuring the homogenization of the component, these were added into manganese acetate solution. To get the precursors of the synthesized spinel cathode material, the resulted solution was further heated at 410ºC with safe stirring at 600 rpm for ~ 8-10 hour. When the solution converted in semisolid, the magnetic stirrer was taken out and heating was continued. The semisolid was grinded manually with glass rod in regular intervals to obtain precursors in dark brownish powder form.

The first precursors of the newly synthesized spinel cathode material were undergone heating treatment for organic impurity removal at 450 ºC for 4 hour and the resulted material was grinded manually with Agate(TM) mortal and

pastel. The powder was calcined in a box furnace, Nabertherm GmbH, Germany, at 850ºC for 14 hour to get phase purity and stable form of material.

The experimental procedure followed for the preparation of the active material powders is schematically represented in figure 1.

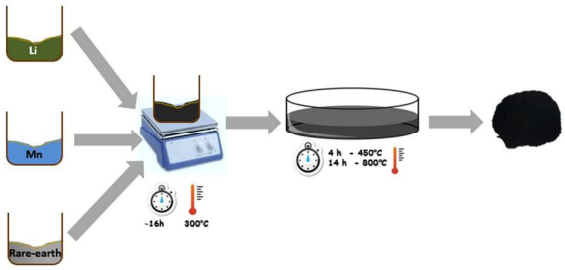

Fig. 1 Schematic representation of the experimental procedure followed for active material powders preparation.

Cathode powder characterization techniques

The physical characterization of phase pure powders was carried out using X-ray diffractogram, Brucker D8 advance, in the range two theta angle 10°-80° with 0.02° per second scan rate in locked coupled mode.

The amounts of the as-synthesized phases were determined by the method of Rietveld using TOPAS-3 software (Bruker AXS Inc.). The method involved fitting of the complete experimental diffraction patterns with calculated profiles and backgrounds. The phases included in the quantification were identified by the EVA software (EVA Software, DIFFRACplus Release 2006, Bruker AXS).

The surface morphology and elemental analysis were studied by Scanning Electron Microscopy (SEM) using Carl Zeiss, Evo special addition. The beam current during surface morphology and energy dispersive x-ray were 80 pA and 200 nA respectively.

High resolution transmission electron microscopy (HRTEM) measurements were performed on a TEM Tecnai G2 instrument by FEI with an accelerating voltage of 200 kV.

Thermogravimetry measurements were performed with a TGA 4000, PerkinElmer. The constant 10 °C per minute heating rate was maintained during heating and cooling from room temperature ~30 °C to 900°C.

Cell preparation and electrochemical measurements

The cathode slurry was prepared with spinel phase pure $LiMn_{1-x}RE_xO_4$ (x=0.05) and $LiMn_2O_4$, carbon Black and polyvinylidiene (PVDF, solvay 5130) into 80:10:10 weight ratio (%), respectively, and N-methylpyrrolidone (NMP, Fluka).

PVDF binder was dissolved in NMP to form the PVDF binder solution and the other components (active material and conductive additive) were dried mixed.

Then, small amounts of solid material (active material and conductive additive) were added to the PVDF binder solution under constant stirring. After adding all solid material, it was left stirring during 2 hours at 1000 rpm to obtain a good dispersion.

The slurry was spread uniformly on 8 mm diameter Al metal grade foil and dried in the furnace at 80 °C for 2 hours.

The prepared cathodes and separator were dried overnight at 90 °C in vacuum.

Li metal foil was used as anode material, Whatman glass microfiber filters (grade GF/A) used as separator and 1M $LiPF_6$ in EC+DMC (1:1) from Solvionic as electrolyte.

Swagelok type-cells (two or three electrodes) were assembled in an home-made argon-filled glove box.

Different electrochemical tests were performed with the cells. Galvanostatic cycling was carried out at different C rates (C10, C/5, C/2 and 1C) between a minimum and a maximum limit of 3.5 and 4.2 V, respectively, using Landt CT2001A Instrument. Electrochemical impedance spectroscopy was measured with an Autolab PGSTAT12 instrument in a frequency range from 1 MHz to 10 mHz with an amplitude of 10 mV. The cyclic voltamogram (CV) was performed in the range from 3.5V to 4.5 V at the scan rate 0.1mV/sec.

Results and discussion

$LiMn_2O_4$ particles doped with different rare earth elements – Gd, Tb, Dy and Yb ($LiMn_{2-x}RE_xO_4$; x=0.05) were synthesized via sol gel route and the effects of rare-earth doping element on crystal structure and electrochemical performance evaluated.

Synthesized powders properties

The morphology of the different $LiMn_2O_4$ powders was determined by SEM images as illustrated in figure 2. The SEM

images of the Tb-doped phases are not shown, as the morphology is similar of the other samples. Independently of the rare-earth doping element, the shape of all the particles is irregular. The average size of the $LiMn_2O_4$ particles (figure 2a) is between 0,5 and 1,4 µm. The rare-earth element doping affects the average size of the powders and for all doped material (figure 2b-d), the average size of the powder is between 0,2 and 0,9 µm, as obtained by image analysis with the Image J Software.

The TEM photographs for $LiMn_2O_4$ and $LiMn_{1.95}Gd_{0.05}O_4$ are presented in figure 2e and f, respectively, in order to properly evaluate particle size. The TEM images show that Gd-doping of LMO decreases the particle size of the powders in comparison to undoped powders. The TEM images of $LiMn_{1.95}Gd_{0.05}O_4$ are representative for the doping with the other elements.

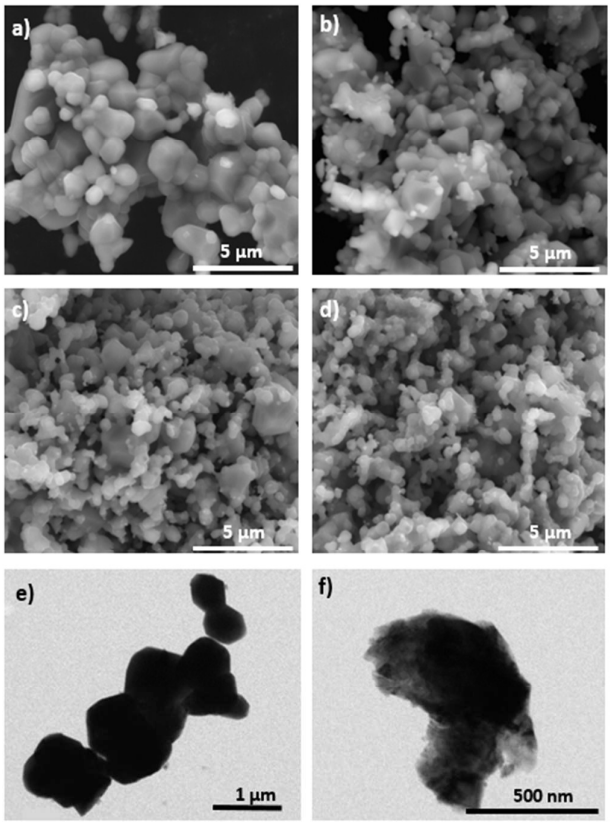

Fig. 2 SEM images of $LiMn_2O_4$ (a), $LiMn_{1.95}Yb_{0.05}O_4$ (b), $LiMn_{1.95}Gd_{0.05}O_4$ (c) and $LiMn_{1.95}Dy_{0.05}O_4$ (d) powders. TEM images of $LiMn_2O_4$ (e) and $LiMn_{1.95}Gd_{0.05}O_4$ (f)

The reduction of the average size of the powders is also observed for the others rare-earth doped materials (figure 2b-d, f). The small sizes achieved with the rare-earth powder doping is an advantage for Li^+ diffusion which enables easier spreading of the electrolyte into the pores and consequently the access to the surfaces of the electrochemically active materials [26]. EDX/SEM was used to analyze the composition of the samples, as shown in figure 3.

EDX results show the presence of Mn, O and the rare earth elements.

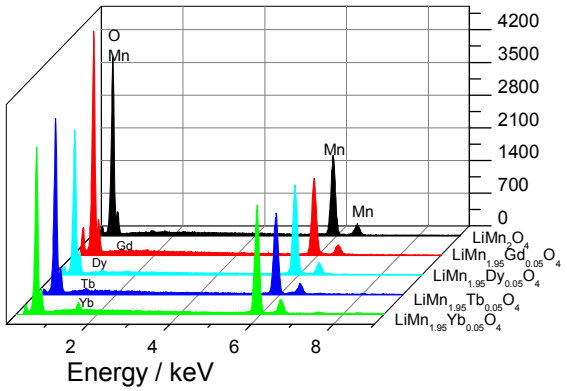

Fig. 3 EDX results for all powders

The results of figure 3 are summarized in table 1 where also a comparison with theoretical values is performed.

Table 1 - EDX Parameters of $LiMn_2O_4$ and $LiMn_{1.95}RE_{0.05}O_4$ (Re: Gd, Yb, Dy, Tb).

Sample description	Elemental Atomic (%)					
	Experimental values			Theoretical values		
	Mn	O	RE	Mn	O	RE
$LiMn_2O_4$	33.71	66.29	0.0	33.33	66.66	0.0
$LiMn_{1.95}Gd_{0.05}O_4$	38.53	60.56	0.91			
$LiMn_{1.95}Yb_{0.05}O_4$	35.93	62.76	1.31			
				32.5	66.66	0.83
$LiMn_{1.95}Dy_{0.05}O_4$	32.77	66.43	0.80			
$LiMn_{1.95}Tb_{0.05}O_4$	33.49	65.50	1.01			

Table 1 shows slight differences of chemical composition for each element (O, Mn and RE) for the different samples. The

presence of the RE elements in $LiMn_2O_4$ particles, by this synthesis method, is also shown in table 1.

The thermal stability of the powders was examined by TGA and results as were shown in figure 4.

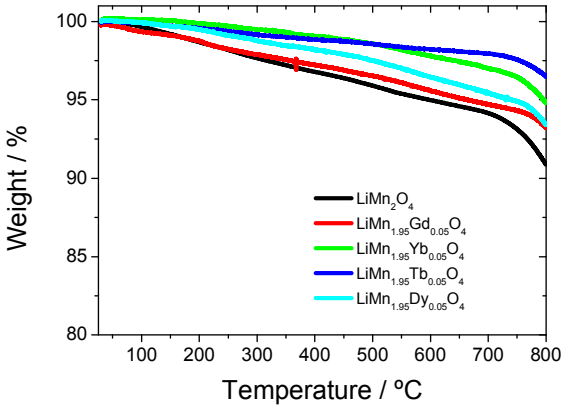

Fig. 4 TGA results for the different powders

For all samples, TGA curves (figure 4) shows a slow weight loss between 300 and 700 ºC. It is also observed that rare-earth elements stabilize the thermal decomposition of $LiMn_2O_4$ particles and the best rare-earth element is terbium which weight decrease is less than 2% at 700ºC. TGA results revealed higher weight changes between 700ºC to 800ºC in all samples due to loss of oxygen and the formation of a stable phase. This loss of oxygen is temperature dependent and was recently shown to be reversible when the temperature is lowered [32].

Figure 5a) shows the refined powder XRD patterns of the as-synthesized samples: $LiMn_2O_4$, $LiMn_{1.95}Gd_{0.05}O_4$, $LiMn_{1.95}Yb_{0.05}O_4$, $LiMn_{1.95}Dy_{0.05}O_4$ and $LiMn_{1.95}Tb_{0.05}O_4$.

The main diffraction peaks of the cubic spinel $LiMn_2O_4$ phase, such as (111), (311), (222) and (400) represented in figure 5a) are detected in all samples, showing that lithium ions occupied tetrahedral 8a sites and manganese occupies octahedral 16d sites.

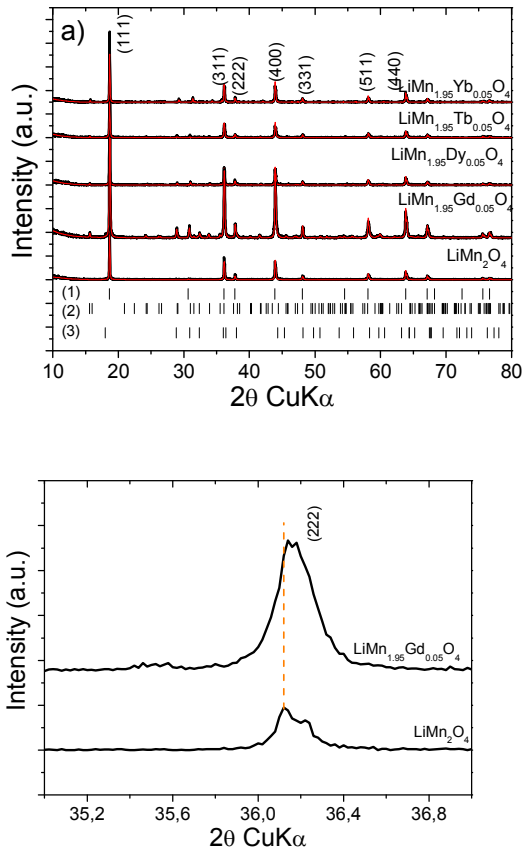

Fig. 5 a) Refined (red: calculated; black: experimental) XRD patterns for $LiMn_2O_4$, $LiMn_{1.95}Gd_{0.05}O_4$, $LiMn_{1.95}Dy_{0.05}O_4$, $LiMn_{1.95}Yb_{0.05}O_4$ and $LiMn_{1.95}Tb_{0.05}O_4$. Vertical bars show the calculated peak positions for (1) $LiREMn_2O_4$, (2) $REMn_2O_5$ and (3) Mn_3O_4. b) Magnified view of the diffraction peak (222) of $LiMn_2O_4$ and $LiMn_{1.95}Gd_{0.05}O_4$.

Figure 5a) shows a very good fit between the observed and calculated data through of Rietveld analyses.

All patterns may be indexed to the Fd3m space group, indicating that rare-earth doping does not affect the formation of the cubic spinel. However, for each rare-earth doping certain amount of impurities is identified and quantified. Within the experimental conditions the formation of the spinel structure is accompanied by crystallization of Mn_3O_4 with haussmanite structure and $REMn_2O_5$. The amount of the two phases varies for the different rare-earth elements but the largest amount (17.09 %) of impurities is detected for the Gd-doped sample. When rare-earth dopants as Tb, Dy and Yb are

used, the total amount of impurities drops and reaches 9.14 % for the Dy-doped sample. Additionally, the samples containing Gd and Tb tend to form larger amount of Mn_3O_4 when compared with the Dy- and Yb- doped phases. These impurities have been also detected in related research works [28, 31].

Figure 5b shows that the inclusion of Gd in the LMO structure leads to a shift to higher angles of the diffraction peak at (222) as well as to a broaden of the peak. These facts indicate that the cell size of the LMO crystals compresses as a result of the incorporation of Gd and proves that the Gd interspaced the Mn sites as expected[33]. This fact was also observed for the other doping elements.

When compared the cell parameter (Lattice constant) of rear doped phases a=8.25 Å, Gd, Dy, Yb, Tb is slightly larger than pristine phase a= 8.24 Å, LMO. This suggests successful incorporation of the dopant element in LMO structure due to bigger ionic radius of the rare earth elements [31].

Electrochemical properties

Electrochemical impedance spectroscopy and CV analysis of the LMO cathodes

Electrochemical impedance spectroscopy (EIS) has been applied to evaluate different processes (Li^+ intercalation/de-intercalation, interfacial resistances, etc) that occur in cathode electrodes and in this work were carried out in the frequency range between 1 MHz and 10 mHz in order to study the effect of rare earth doping on the electrical properties of the $LiMn_2O_4$ cathode materials.

Figure 6a shows the EIS spectra (Nyquist plot) in discharged state after CV measurements. All Nyquist plot shows a semicircle in the high frequency range attributed to the electron transfer process as well as an inclined line at low frequency that reflects Li^+ solid-state diffusion within the electrode [34].

The EIS spectra reflect the steps of the Li^+ intercalation process, including the diffusion of Li^+ in solution (ohmic resistance, i.e, liquid electrolyte resistance), Li^+ migration through the surface film of cathode material (solid electrolyte interface (SEI) resistance), charge-transfer for Li^+ intercalation (charge-transfer resistance), diffusion of Li^+ in the solid phase (Warburg impedance) and occupation of Li in the lattice [35, 36].

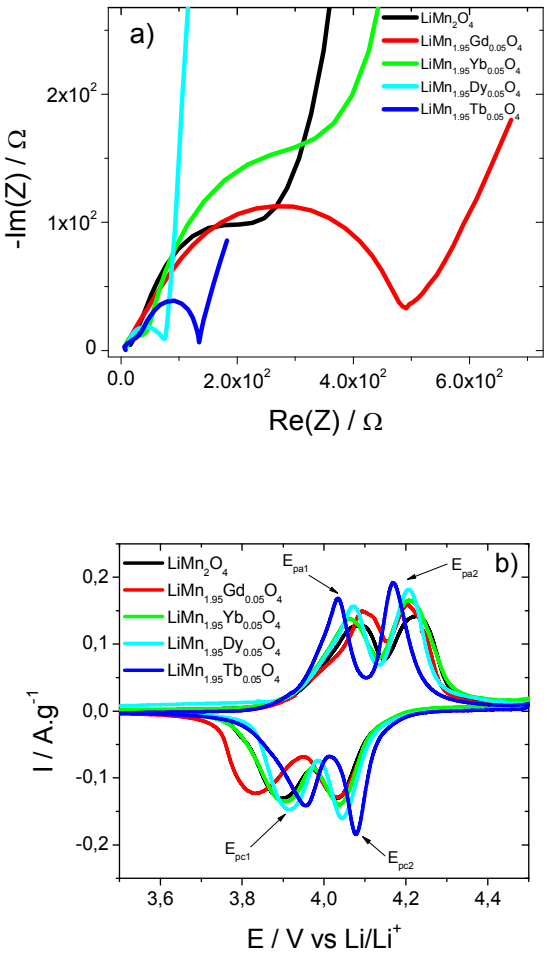

Fig. 6 For all samples: a) Impedance spectra and b) Cyclic voltammetric curves

Also figure 6a shows that the ohmic resistance (liquid electrolyte resistance), given by the intercept the Z_{re}-axis at high frequency is not influenced by the rare earth doping. On the other hand, the total resistance (diameter of the semicircle in the medium frequency) that correspond to the sum of solid electrolyte interface (SEI) and the charge-transfer resistances process in the cathode material already is affected by the rare earth doping.

Thus, the impedance data of the samples show an overall improvement of the electrical conductivity in the following

order: Dy (75Ω) > Tb (133 Ω) > LMO (455 Ω) > Gd (488 Ω) > Yb (679 Ω).

Cyclic voltammetry (CV) studies have been performed to analyze the electrochemical intercalation/de-intercalation of the cathode material as it is shown in figure 6b for the same scan rate.

Figure 6b shows two pairs of separated redox peaks (reversible oxidation/reduction peaks) that characterize Li^+ insertion into and de-intercalation from the lattice, i.e, lithium ions are extracted from and inserted into the spinel phase in a two-step process [26, 37, 38].

The first peak is attributed to the removal of Li^+ from half of the tetrahedral sites where Li–Li interaction exists, whereas the second peak is ascribed to the removal of Li^+ from the other tetrahedral sites in which such interaction does not exist [39].

Independently of the rare earth doping, anodic and cathodic peaks are observed corresponding to the charge and discharge processes, respectively (figure 6b).

The main characteristics of the CV results are summarized in Table 2. The symbols are defined as follows: E_{pa}: anodic peak potential, E_{pc}: cathodic peak potential. The numbers 1 and 2 denote the redox couple at lower and higher potential, respectively

Taking into account the results in table 2, it is observed that ΔE_{p1} and ΔE_{p2} are higher than the ideal condition (ΔE_p=0) which indicate that $Mn^{3+} \leftrightarrow Mn^{4+}$ is controlled by insertion/disinsertion of Li^+ in the cathode electrodes independently of the sample [40].

Table 2 - Electrochemical parameters from CV for all samples

Sample description	Potential values / V					
	E_{pa1}	E_{pa2}	E_{pc1}	E_{pc2}	ΔE_{p1}	ΔE_{p2}
$LiMn_2O_4$	4.09	4.23	3.89	4.03	0.2	0.2
$LiMn_{1.95}Gd_{0.05}O_4$	4.10	4.21	3.82	4.03	0.28	0.18
$LiMn_{1.95}Yb_{0.05}O_4$	4.06	4.21	3.90	4.04	0.16	0.17
$LiMn_{1.95}Dy_{0.05}O_4$	4.07	4.21	3.92	4.04	0.15	0.17
$LiMn_{1.95}Tb_{0.05}O_4$	4.03	4.17	3.96	4.08	0.07	0.09

The lower values of ΔE_{p1} and ΔE_{p2} for samples doping of rare earth in comparison to pristine LMO except for ΔE_{p1} of $LiMn_{1.95}Gd_{0.05}O_4$ are due to the particle size as is observed in the SEM images. The particle size affects the diffusion paths of lithium-ion, low particle sizes decreasing the diffusion behavior of lithium-ion through the active materials of the cathode electrodes which means a low ΔE_p [41].

Charge-Discharge Performance

Figure 7 a) shows the charge–discharge curves at room temperature as a function of cycle number at C10.

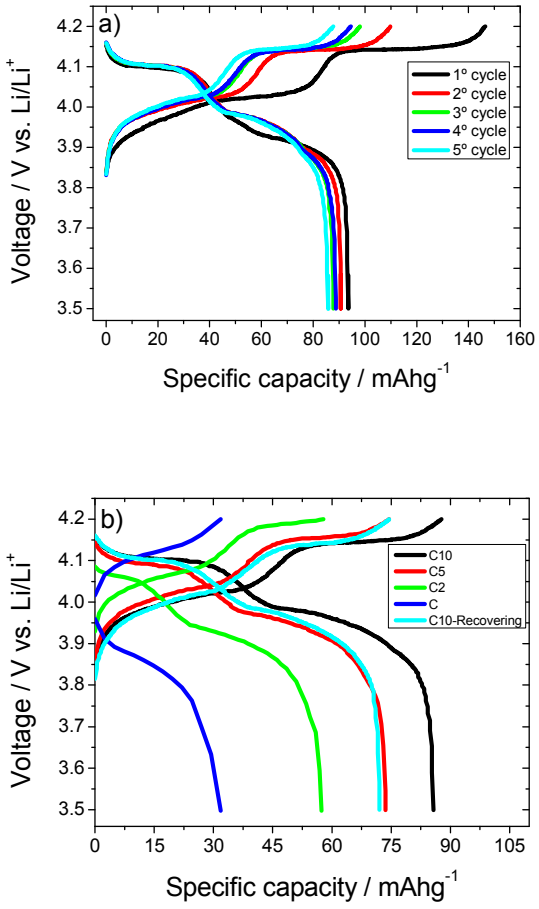

Fig. 7 Charge-Discharge curves of the LMO cathodes: a) at C10 as a function of cycle number and b) C10 to C for the 5th cycle.

Independently of the cycle number, two plateaus are observed in the charge-discharge curves. The reason for this fact is due to a two-step reduction and oxidation process, which is a characteristic of $LiMn_2O_4$ spinel structure [42] that correspond to the two pairs of redox peaks in the CV results (figure 6b) [38]. These plateaus are attributed to orderly intercalating Li ions in

tetrahedral (8a) sites at 4.1 V and disorderly intercalating lithium ions at 3.9 V [43].

The $LiMn_2O_4$ cathode material showed the highest discharge capacity (85.6 mAh/g), but after 5 cycles it is observed a 84% capacity retention (figure 7a).

The charge–discharge curves of the $LiMn_2O_4$ electrode at various current rates are shown in figure 7b). The two plateaus are observed in figure 7b), independently of the scan rate. Figure 7b) shows that when the discharge scan rate increases, the discharge potential profiles decrease. It delivers discharge capacities of 87.5 mAh g^{-1}, 65.1 mAh g^{-1}, 33.8 mAh g^{-1} and 31.7 mAh g^{-1} at C10, C5, C2 and C, respectively, due to increased polarization at higher current rates [44].

Figure 8 shows the charge–discharge curves at room temperature for all samples at C10 (figure 8a) and C (figure 8b) at the 5th cycle.

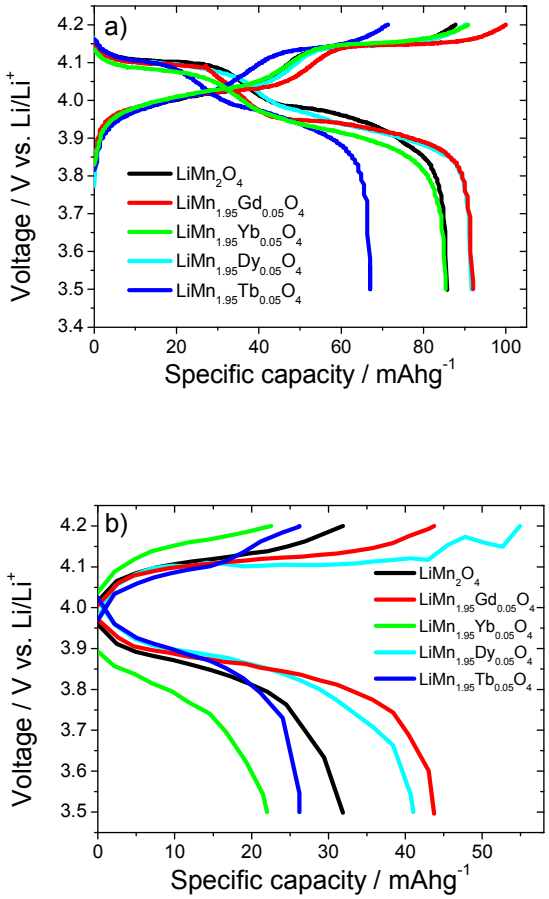

Fig. 8 Charge-Discharge curves for all cathodes: a) at C10 and b) C for the 5th cycle.

In figure 8 at a scan rate of C10 (figure 8a) and C (figure 8b) shows that the doping with rare earth elements affects the charge-discharge performance of the $LiMn_2O_4$ cathode material. In figure 8b) at C, separation of the two discharge plateaus gradually becomes blurred and the plateau voltages shifts to lower values due to increased cell polarization [38].

The discharge capacity shows for cathodes at C10 ($LiMn_2O_4$: 85.6 mAh g^{-1}; $LiMn_{1.95}Gd_{0.05}O_4$: 91.9 mAh g^{-1}; $LiMn_{1.95}Dy_{0.05}O_4$: 88.3 mAh g^{-1}; $LiMn_{1.95}Yb_{0.05}O_4$: 85.3 mAh g^{-1}; $LiMn_{1.95}Tb_{0.05}O_4$: 67.1 mAh g^{-1}; respectively) higher values than for the cathode material at C (; $LiMn_{1.95}Dy_{0.05}O_4$: 41.0 mAh g^{-1}; $LiMn_{1.95}Gd_{0.05}O_4$: 43.8 mAh g^{-1}; $LiMn_2O_4$: 31.7 mAh g^{-1}; $LiMn_{1.95}Tb_{0.05}O_4$: 26.4 mAh g^{-1}; $LiMn_{1.95}Yb_{0.05}O_4$: 22.2 mAh g^{-1}; respectively) due to the electrochemical polarization.

The rare earth element doping thus affects the discharge capacity value of $LiMn_2O_4$ cathode material as the lower particle size enhances the electrochemical efficiency through the intercalation and de-intercalation processes of the Li^+ ions due to the large surface area of the particles.

Figure 9 shows the rate performance of all samples in the charge and discharge process, respectively.

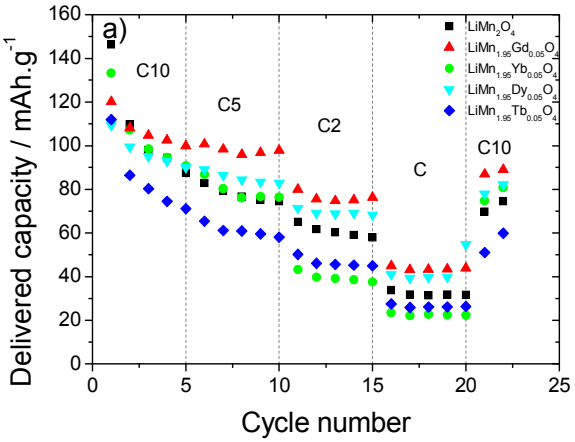

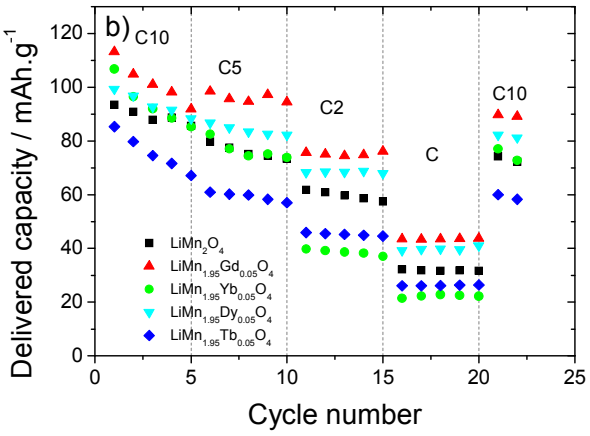

Fig. 9 Rate performances of all samples in: a) charge process and b) discharge process

Independently of the rare earth element, figure 9 shows charge and discharge capacity and excellent cycling stability, in particular at C rate. The cycling performance presents fading when the scan rate increases but exhibits excellent capacity value at C10 recovering cycle.

Figure 9 shows that the delivered capacity value generally stabilizes after the first five cycles, independently of the sample.

The coulombic efficiency (CE), related to reversibility process is approximately 96% for all cathode material with doping of rare earth elements which shows lower polarization for all scan rates in comparison to $LiMn_2O_4$ cathode material (CE=80% for C10 scan rate).

Generally, the charge-discharge performance shows an improvement as a function of rare earth doping in comparison of pristine $LiMn_2O_4$ except for terbium (Tb) and ytterbium (Yb) and presents following order: Gd > Dy > Tb > Yb.

Thus, beyond the particle size, the reason for this fact is related to the atomic radius of the rare earth elements. It is observed that charge-discharge performance of $LiMn_2O_4$ doping of rare earth increases with increasing of atomic radius of the rare earth.

The delivered discharge capacity, normalized with respect to the nominal one, vs. current rate dependence for all samples is displayed in figure 10a.

In all samples, it is observed that capacity retention decreases with increasing scan rate due to the Li^+ ion diffusion process in the active material of the cathode material.

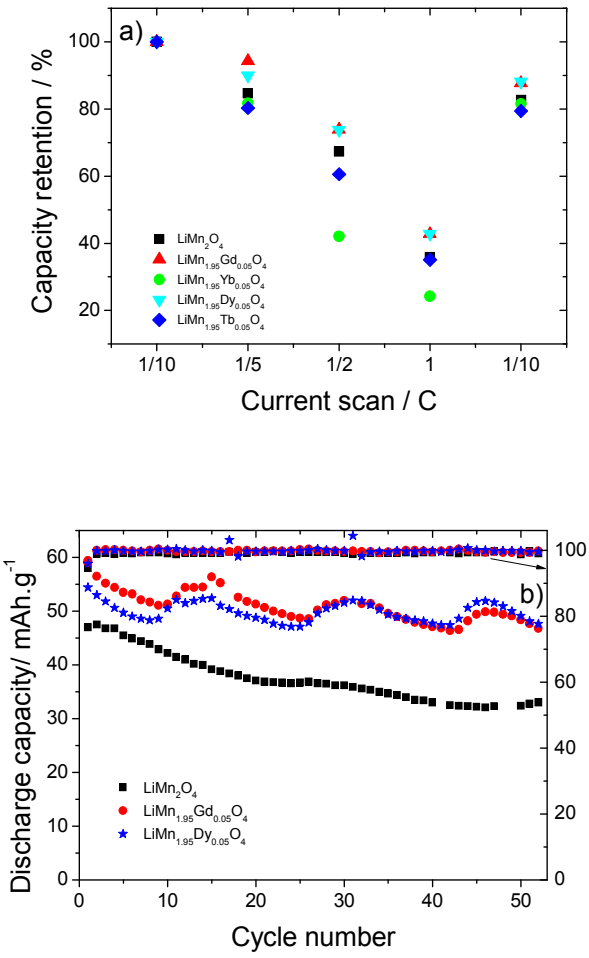

Fig. 10 a) Capacity retention vs. current rate dependence for the different samples and b) cycle performance of $LiMn_2O_4$, $LiMn_{1.95}Gd_{0.05}O_4$ and $LiMn_{1.95}Dy_{0.05}O_4$ at C2.

However, the rare earth doping increases the capacity retention of $LiMn_2O_4$ cathode materials except for ytterbium (Yb) in comparison with pristine $LiMn_2O_4$.

For all samples, the discharge capacity values are 43.6 mAh g^{-1}, 39.7 mAh g^{-1}, 31.8 mAh g^{-1}, 26.2 mAh g^{-1} and 22.3 mAh g^{-1} after 20 cycles for $LiMn_{1.95}Gd_{0.05}O_4$, $LiMn_{1.95}Dy_{0.05}O_4$, $LiMn_2O_4$, $LiMn_{1.95}Tb_{0.05}O_4$ and $LiMn_{1.95}Yb_{0.05}O_4$, respectively, corresponding to a capacity retention of 42.8%, 42.8%, 35.9%, 35.1% and 24.2%, respectively.

Differences of the capacity retention (figure 10a) on cycling are attributed to superior structural stability due to rare earth doping with gadolinium (Gd), terbium (Tb) and dysprosium (Dy), with respect to pristine $LiMn_2O_4$.

Taking into account that rare earth doping with gadolinium (Gd) and dysprosium (Dy) show higher capacity retention in comparison to pristine $LiMn_2O_4$, figure 10b reveals the cycle stability for these samples in the range of 3.5V to 4.5 V at a current of C2.

After 50 cycles, the discharge capacity are 49.1 mAh g^{-1},48.4 mAh g^{-1} and 32.4 mAh g^{-1} for $LiMn_{1.95}Dy_{0.05}O_4$, $LiMn_{1.95}Gd_{0.05}O_4$ and $LiMn_2O_4$, respectively, demonstrating that $LiMn_{1.95}Dy_{0.05}O_4$ shows the best cycle stability.

The reason for this wave-like fluctuations of the discharge capacity values observed in figure 10b are related to daily fluctuation of the ambient temperature, leading to variations in battery temperature.

The charge–discharge capacity for different cycles at C2 is presented in Table 3 for $LiMn_2O_4$, $LiMn_{1.95}Gd_{0.05}O_4$ and $LiMn_{1.95}Dy_{0.05}O_4$.

Table 3 - Charge and discharge capacities for LiMn2O4, LiMn1.95Gd0.05O4 and LiMn1.95Dy0.05O4 at C2 at room temperature

Capacity and capacity fade	$LiMn_2O_4$	$LiMn_{1.95}Gd_{0.05}O_4$	$LiMn_{1.95}Dy_{0.05}O_4$
First charge capacity (±3) mAh.g^{-1}	49.7	61.9	56.5
First discharge capacity (±3) mAh.g^{-1}	47	59.4	54.4
2nd and 50th discharge capacity (±3) mAh.g^{-1}	47.5; 32.4	56.5; 48.4	53; 49.1
Initial capacity loss (%)	5.4	4	3.7
Capacity fade: 50 cycles (%)	32	14	7

The initial charge and discharge capacities (Table 3) indicate enhanced capacity for the doped $LiMn_2O_4$ cathode electrodes, attributed to the addition of Gd^{3+} and Dy^{3+} in the doped samples, respectively.

The capacity fade after 50 cycles is just 7% for $LiMn_{1.95}Dy_{0.05}O_4$ and 14% for $LiMn_{1.95}Gd_{0.05}O_4$, in comparison to the value of 32% observed for $LiMn_2O_4$. The charge-discharge profiles of the $LiMn_2O_4$, $LiMn_{1.95}Gd_{0.05}O_4$ and $LiMn_{1.95}Dy_{0.05}O_4$ electrodes for the 5th, 25th and 45th cycles are shown as supplementary information, showing the stability of the developed cathodes.

Thus, due to the improved performance with respect to capacity fade indicate that $LiMn_2O_4$ doped with Gd and Dy provides good electrochemical performance for the development of cathodes for lithium-ion batteries applications.

Conclusions

The spinel $LiMn_2O_4$ powder doping with different rare earth has been successfully achieved by a sol-gel method. The rare earth elements used in this work are gadolinium (Gd), terbium (Tb), dysprosium (Dy) and ytterbium (Yb) with the same amount (RE=0.05).

The rare earth doing decrease the powder size of the active material, does not affect the formation of a cubic spinel structure and affects the overall electrical conductivity, the latter improving for Dy-doped and Tb-doped LMO cathodes.

In relation of CV results, the typical two pairs peaks is detected for all samples. The charge-discharge curves show a significant high discharge capability value at room temperature with rare earth doping. The discharge capacities values are 43.6 mAh g^{-1}, 39.7 mAh g^{-1}, 31.8 mAh g^{-1}, 26.2 mAh g^{-1} and 22.3 mAh g^{-1} after 20 cycles for $LiMn_{1.95}Gd_{0.05}O_4$, $LiMn_{1.95}Dy_{0.05}O_4$, $LiMn_2O_4$, $LiMn_{1.95}Tb_{0.05}O_4$ and $LiMn_{1.95}Yb_{0.05}O_4$, respectively, corresponding to a capacity retention of 42.8%, 42.8%, 35.9%, 35.1% and 24.2%.

After 50 cycles at C2, the capacity fade is 7% for $LiMn_{1.95}Dy_{0.05}O_4$ and 14% for $LiMn_{1.95}Gd_{0.05}O_4$ in comparison to the value of 32% observed for $LiMn_2O_4$.

The best rare earth doping elements are gadolinium (Gd) and dysprosium (Dy) which exhibit better electrochemical cycling performance in comparison to pristine $LiMn_2O_4$.

Taking account these results, $LiMn_{1.95}Dy_{0.05}O_4$ and $LiMn_{1.95}Gd_{0.05}O_4$ are proposed as excellent active materials for cathodes in rechargeable lithium-ion battery applications.

Acknowledgements

This work is funded by FCT – Fundação para a Ciência e a Tecnologia, in the framework of the PTDC/CTM-ENE/5387/2014 and PTDC/EEI-SII/5582/2014 projects. A. G. and C.M.C. also thanks the FCT for the grant SFRH/BD/90313/2012 and SFRH/BPD/112547/2015, respectively. The authors thank funding from the FCT under the Indo-Portuguese program of cooperation in science and technology (INT/Portugal/P-02/2013) 2014-2016. The fellowship from MHRD, Govt. of India was acknowledged for Pura Ram. The authors thank financial support from the Basque Government Industry Department under the ELKARTEK Program. SLM thanks the Diputación de Bizkaia for financial support under the Bizkaia Talent program; European Union's Seventh Framework Programme; Marie Curie Actions – People; Grant agreement nº 267230.

Notes and references

1 D. Assmann, Renewable Energy: A Global Review of Technologies, Policies and Markets, Taylor & Francis, 2012.
2 I. Galarraga and A. Markandya, Handbook of Sustainable Energy, Edward Elgar Publishing, Incorporated, 2011.
3 B. Sorensen, Renewable Energy: Physics, Engineering, Environmental Impacts, Economics & Planning, Elsevier Science, 2010.
4 R. Huggins, Advanced Batteries: Materials Science Aspects, Springer, 2008.
5 M. Wakihara and O. Yamamoto, Lithium Ion Batteries: Fundamentals and Performance, Wiley, 2008.
6 B. Scrosati and J. Garche, *Journal of Power Sources*, 2010, **195**, 2419-2430.
7 J. M. Tarascon and M. Armand, *Nature*, 2001, **414**, 359-367.
8 H. Jiang, H. Zhang, Y. Fu, S. Guo, Y. Hu, L. Zhang, Y. Liu, H. Liu and C. Li, *ACS Nano*, 2016, **10**, 1648-1654.
9 J. W. Fergus, *Journal of Power Sources*, 2010, **195**, 939-954.
10 S. B. Chikkannanavar, D. M. Bernardi and L. Liu, *Journal of Power Sources*, 2014, **248**, 91-100.
11 C. M. Hayner, X. Zhao and H. H. Kung, *Annual Review of Chemical and Biomolecular Engineering*, 2012, **3**, 445-471.
12 K. Y. Cho, Y. I. Kwon, J. R. Youn and Y. S. Song, *Materials Research Bulletin*, 2013, **48**, 2922-2926.
13 Y. Fu, H. Jiang, Y. Hu, L. Zhang and C. Li, *Journal of Power Sources*, 2014, **261**, 306-310.
14 E. Antolini, *Solid State Ionics*, 2004, **170**, 159-171.
15 S. Lee, Y. Cho, H.-K. Song, K. T. Lee and J. Cho, *Angewandte Chemie International Edition*, 2012, **51**, 8748-8752.
16 S. Lee, G. Yoon, M. Jeong, M.-J. Lee, K. Kang and J. Cho, *Angewandte Chemie International Edition*, 2015, **54**, 1153-1158.
17 W.-J. Zhang, *Journal of Power Sources*, 2011, **196**, 2962-2970.
18 M.-J. Lee, S. Lee, P. Oh, Y. Kim and J. Cho, *Nano Letters*, 2014, **14**, 993-999.
19 Q. Liu, S. Wang, H. Tan, Z. Yang and J. Zeng, *Energies*, 2013, **6**, 1718.
20 D. K. Kim, P. Muralidharan, H.-W. Lee, R. Ruffo, Y. Yang, C. K. Chan, H. Peng, R. A. Huggins and Y. Cui, *Nano Letters*, 2008, **8**, 3948-3952.
21 Z.-m. Yu and L.-c. Zhao, *Transactions of Nonferrous Metals Society of China*, 2007, **17**, 659-664.
22 M. Wohlfahrt-Mehrens, C. Vogler and J. Garche, *Journal of Power Sources*, 2004, **127**, 58-64.
23 T. Inoue and M. Sano, *Journal of The Electrochemical Society*, 1998, **145**, 3704-3707.
24 H. Jiang, Y. Fu, Y. Hu, C. Yan, L. Zhang, P. S. Lee and C. Li, *Small*, 2014, **10**, 1096-1100.
25 Y. Fu, H. Jiang, Y. Hu, Y. Dai, L. Zhang and C. Li, *Industrial & Engineering Chemistry Research*, 2015, **54**, 3800-3805.
26 Y. Cai, Y. Huang, X. Wang, D. Jia, W. Pang, Z. Guo, Y. Du and X. Tang, *Journal of Power Sources*, 2015, **278**, 574-581.
27 Y. Chae, J. K. Lee and W. Choi, *Journal of Electroanalytical Chemistry*, 2014, **730**, 20-25.
28 S. C. Han, S. P. Singh, Y.-h. Hwang, E. G. Bae, B. K. Park, K.-S. Sohn and M. Pyo, *Journal of The Electrochemical Society*, 2012, **159**, A1867-A1873.
29 S. Balaji, T. M. Chandran and D. Mutharasu, *Ionics*, 2012, **18**, 549-558.
30 H. Sun, Y. Chen, C. Xu, D. Zhu and L. Huang, *J Solid State Electrochem*, 2012, **16**, 1247-1254.
31 D. K. Lee, S. C. Han, D. Ahn, S. P. Singh, K.-S. Sohn and M. Pyo, *ACS Applied Materials & Interfaces*, 2012, **4**, 6842-6848.
32 D. G. Fauteux, A. Massucco, J. Shi and C. Lampe-O¨Nnerud, *Journal of Applied Electrochemistry*, 1997, **27**, 543-549.
33 K. Feng, Y. Cheng, M. Wang, H. Zhang, X. Li and H. Zhang, *Journal of Materials Chemistry A*, 2015, **3**, 19469-19475.
34 H. M. Wu, J. P. Tu, Y. F. Yuan, Y. Li, X. B. Zhao and G. S. Cao, *Materials Chemistry and Physics*, 2005, **93**, 461-465.
35 D. Lu, W. Li, X. Zuo, Z. Yuan and Q. Huang, *The Journal of Physical Chemistry C*, 2007, **111**, 12067-12074.
36 C. L. Tan, H. J. Zhou, W. S. Li, X. H. Hou, D. S. Lü, M. Q. Xu and Q. M. Huang, *Journal of Power Sources*, 2008, **184**, 408-413.
37 X. H. Hu, X. P. Ai, H. X. Yang and S. X. Li, *Journal of Power Sources*, 1998, **74**, 240-243.
38 Y. Deng, Y. Zhou, Z. Shi, X. Zhou, X. Quan and G. Chen, *Journal of Materials Chemistry A*, 2013, **1**, 8170-8177.
39 P. Ragupathy, H. N. Vasan and N. Munichandraiah, *Materials Chemistry and Physics*, 2010, **124**, 870-875.
40 M. A. Kiani, M. F. Mousavi and M. S. Rahmanifar, *Int. J. Electrochem. Sci.*,, 2011, **6**, 15.
41 Y. Iriyama, M. Inaba, T. Abe and Z. Ogumi, *Journal of Power Sources*, 2001, **94**, 175-182.
42 C.-H. Lu and S. K. Saha, *Materials Science and Engineering: B*, 2001, **79**, 247-250.
43 H. Şahan, H. Göktepe and Ş. Patat, *Journal of Materials Science & Technology*, 2011, **27**, 415-420.
44 Y. Ding, J. Li, Y. Zhao and L. Guan, *Materials Letters*, 2012, **68**, 197-200.

Table of Contents (TOC)

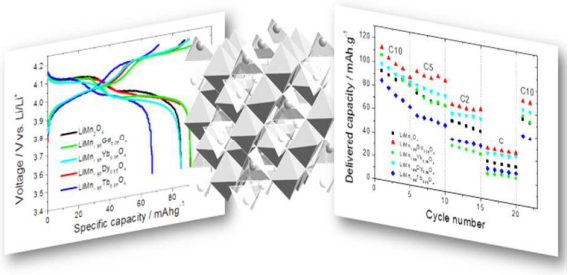

$LiMn_2O_4$ has been doped with different rare earth elements in order to improve battery cycling performance and reduce capacity fading.